Process-dependent anisotropic thermal conductivity of laser powder bed fusion AlSi10Mg: impact of microstructure and aluminum-silicon interfaces

Arad Azizi, Fatemeh Hejripour, Jacob A. Goodman and Piyush A. Kulkarni
Department of Mechanical Engineering, Thomas J. Watson School of Engineering and Applied Science, Binghamton University, Binghamton, New York, USA, and
Xiaobo Chen, Guangwen Zhou and Scott N. Schiffres
Department of Mechanical Engineering, Materials Science and Engineering Program, Thomas J. Watson School of Engineering and Applied Science, Binghamton University, Binghamton, New York, USA

Abstract

Purpose – AlSi10Mg alloy is commonly used in laser powder bed fusion due to its printability, relatively high thermal conductivity, low density and good mechanical properties. However, the thermal conductivity of as-built materials as a function of processing (energy density, laser power, laser scanning speed, support structure) and build orientation, are not well explored in the literature. This study aims to elucidate the relationship between processing, microstructure, and thermal conductivity.

Design/methodology/approach – The thermal conductivity of laser powder bed fusion (L-PBF) AlSi10Mg samples are investigated by the flash diffusivity and frequency domain thermoreflectance (FDTR) techniques. Thermal conductivities are linked to the microstructure of L-PBF AlSi10Mg, which changes with processing conditions. The through-plane exceeded the in-plane thermal conductivity for all energy densities. A co-located thermal conductivity map by frequency domain thermoreflectance (FDTR) and crystallographic grain orientation map by electron backscattered diffraction (EBSD) was used to investigate the effect of microstructure on thermal conductivity.

Findings – The highest through-plane thermal conductivity (136 ± 2 W/m-K) was achieved at 59 J/mm^3 and exceeded the values reported previously. The in-plane thermal conductivity peaked at 117 ± 2 W/m-K at 50 J/mm^3. The trend of thermal conductivity reducing with energy density at similar porosity was primarily due to the reduced grain size producing more Al-Si interfaces that pose thermal resistance. At these interfaces, thermal energy must convert from electrons in the aluminum to phonons in the silicon. The co-located thermal conductivity and crystallographic grain orientation maps confirmed that larger colonies of columnar grains have higher thermal conductivity compared to smaller columnar grains.

Practical implications – The thermal properties of AlSi10Mg are crucial to heat transfer applications including additively manufactured heatsinks, cold plates, vapor chambers, heat pipes, enclosures and heat exchangers. Additionally, thermal-based nondestructive testing methods require these properties for applications such as defect detection and simulation of L-PBF processes. Industrial standards for L-PBF processes and components can use the data for thermal applications.

Originality/value – To the best of the authors' knowledge, this paper is the first to make coupled thermal conductivity maps that were matched to microstructure for L-PBF AlSi10Mg aluminum alloy. This was achieved by a unique in-house thermal conductivity mapping setup and relating the data to local SEM EBSD maps. This provides the first conclusive proof that larger grain sizes can achieve higher thermal conductivity for this processing method and material system. This study also shows that control of the solidification can result in higher thermal conductivity. It was also the first to find that the build substrate (with or without support) has a large effect on thermal conductivity.

Keywords Thermal conductivity, Laser powder bed fusion (L-PBF) additive manufacturing, AlSi10Mg aluminum alloy, Thermal transport in additive manufacturing, Nondestructive testing (NDT), Nondestructive evaluation (NDE)

Paper type Research paper

1. Introduction

The low density and high thermal diffusivity make aluminum alloys desirable for thermal management applications such as lightweight heat exchangers and heat sinks for electronic devices (Collins *et al.*, 2019; Dokken and Fronk, 2018; Lu *et al.*, 1998; T'Joen *et al.*, 2010; Tseng *et al.*, 2019; Yeh, 1995). The high strength-to-weight ratio and corrosion resistance of aluminum has led to diverse aerospace and automotive applications (Liu *et al.*, 2020; Meier *et al.*, 2018). While laser powder bed fusion (L-PBF) enables fabrication of freeform high performance heat transfer devices (Alexandersen *et al.*, 2018; Alihosseini *et al.*, 2020; Fasano *et al.*, 2016; Kirsch and

The current issue and full text archive of this journal is available on Emerald Insight at: **https://www.emerald.com/insight/1355-2546.htm**

Rapid Prototyping Journal
 [ISSN 1355-2546]
[DOI 10.1108/RPJ-09-2022-0290]

Received 6 September 2022
Revised 28 October 2022
5 December 2022
Accepted 7 December 2022

Thole, 2017; Moon *et al.*, 2020), there is a need to study the thermal conductivities of these L-PBF materials, which are poorly understood (Simmons *et al.*, 2020).

The extreme local heat fluxes ($\sim 10^{11}$ W/m^2), cooling rates ($\sim 10^6$ K/s), thermal gradients ($\sim 10^6$ K/m) and melt pool dynamics (keyholing, void trapping, spattering, vaporization, oxidation) of L-PBF lead to material properties quite different from conventionally wrought or cast aluminum alloys (Aboulkhair *et al.*, 2019; EOS GmbH - Electro Optical System, 2014; Jawade *et al.*, 2020; Kempen *et al.*, 2012; Kimura *et al.*, 2017; Raus *et al.*, 2017). For instance, the tensile strength of as-built L-PBF Al6066 can be even greater than its wrought counterpart depending on the used energy density (Fulcher *et al.*, 2014; Maamoun *et al.*, 2018). In some aluminum alloys, hot tearing produces many internal cracks due to large stresses upon cooling (Mathers, 2002), which can be reduced with the addition of Si to the alloy that lower the melting point and keeps the alloy in the mushy state over a larger temperature range (Kempen *et al.*, 2012; Di Sabatino and Arnberg, 2009).

While Si is necessary to prevent hot-tearing, the Si content dramatically reduces the thermal conductivity of L-PBF as-built material, reducing from ~200 W/m-K for 0 Wt.% Si down to 105 W/m-K for 20 Wt.% Si (Kimura *et al.*, 2017), similar to trends for cast Al-Si alloys (dropping from 171 to 153 W/m-K as Si increases from 1 to 1.5 Wt.%) (Chen *et al.*, 2017; Shin *et al.*, 2014). As the Al-Si solidifies, it segregates into α-Al matrix and Si. The as-built microstructure is often cellular with Si enveloping the Al grains, which lowers thermal conductivity (Kimura *et al.*, 2017; Silbernagel *et al.*, 2018), as thermal energy must convert from being predominantly carried by electrons in Al to being carried by phonons (quantized lattice vibrations) in Si (Yang *et al.*, 2018). Heat treatment of Al-Si alloys evolves the Si shells into spheroidal precipitates, reducing the thermal interfaces encountered, thus improving thermal conductivity (Sélo *et al.*, 2020; Yang *et al.*, 2018).

In the L-PBF process, rapid solidification forms a textured microstructure with cellular and columnar dendritic aluminum structure and inter-granular silicon and magnesium precipitates (Liu *et al.*, 2019b; Silbernagel *et al.*, 2018; Van Cauwenbergh *et al.*, 2021). The Si cellular walls impede thermal conductivity of L-PBF parts. For such type of material with complex microstructure, it could be very important to detect the correlation of microstructure and thermal conductivity.

Among Al-Si alloys for L-PBF, AlSi10Mg with an average of 10 Wt.% Si is commonly used by industry due to processability, high strength-to-weight-ratio and corrosion resistance (Bagherifard *et al.*, 2018; Fathi *et al.*, 2019; Read *et al.*, 2015). Previously, thermal conductivity of L-PBF AlSi10Mg solid parts and lattices were measured as a function of temperature and heat treatment (Butler *et al.*, 2021; Kim, 2021; Sélo *et al.*, 2020; Yang *et al.*, 2018). It was observed the as-built AlSi10Mg has considerably lower thermal conductivity compared to pure aluminum and heat treated samples due to phonon and electron scattering sites as a result of Si and Mg alloying (Yang *et al.*, 2018). Heat treatment results in improved thermal conductivities of 18–41% compared to pre-treatment due to the precipitation of silicon into spheres rather than inter-granular films. No considerable difference in the post-heat treated thermal conductivities were observed for annealing temperatures from 300 to 500°C (Butler *et al.*, 2021). However, the literature still lacks in-depth study of as-built L-PBF AlSi10Mg thermal conductivity as a function of laser processing conditions (energy density, laser power, laser scanning speed, support structure) and build orientation, which the present study addresses.

Recently, the bulk thermal conductivity of laser powder bed fusion AlSi10Mg was investigated using an apparatus based on the steady state guard hot-plate method (Elkholy *et al.*, 2022). This literature varied energy density by holding all build variables fixed except laser scanning speed. Notably, this literature "propose[d] that the melt pool boundaries and the relative density are the main reasons for the thermal conductivity change." As will be subsequently shown by our co-located thermal and crystallographic maps, we find evidence that directly contradicts this paper's hypothesis. Elkholy *et al.* (2022) also states that these melt pool boundaries reduce heat transfer primarily through phonon scattering, while we attribute the dominant source to electron-phonon coupling at the Al-Si interfaces.

The existing literature has not well examined the role Al-Si interfaces play in L-PBF AlSi10Mg thermal transport. The literature has also provided contradicting explanations regarding the source of L-PBF thermal conductivity reductions at low porosities (Elkholy *et al.*, 2022; Yang *et al.*, 2018). Addressing these knowledge gaps, we make the first coupled thermal conductivity maps for L-PBF AlSi10Mg alloy that were matched to microstructure, and only the second to do so for any additively manufactured material. We were able to achieve this with a unique in-house thermal conductivity mapping setup that was co-located to crystallographic maps. These measurements provide the first conclusive proof that larger grains achieve higher thermal conductivity for this processing method and material system. It was also the first to find that the build substrate (with support or no support) has a large effect on thermal conductivity. This information has important implications for thermal-based nondestructive testing that can use local thermal conductivity information to infer local microstructure and defects (Schiffres *et al.*, 2020), modeling the print process and residual stresses, and understanding properties of printed parts with thermal applications, especially those that cannot be heat treated (e.g. embedded sensors or print onto electronic chips (Azizi, 2019a, 2019b, 2022; Azizi and Schiffres, 2018; Schiffres and Azizi, 2021)).

2. Material and methods

2.1 Materials and processing technique

Samples were made in an EOS M290 L-PBF system located in Binghamton's Additive Manufacturing Core using AlSi10Mg powder sourced from EOS (EOS GmbH - Electro Optical System, 2014). Non-virgin powder was used for this study. The powder size distribution was measured via a particle size analyzer (Beckman Coulter, Model LS 13 320) with D10 of 24.38 μm, D50 of 49.27 μm, D90 of 72.08 μm (see Supplementary Information, Section 4). The layer thickness and hatch distance were fixed at 30 and 190 μm for all samples, respectively.

The laser melting of aluminum alloys is directly dependent on the material thermal conductivity and laser absorption. These two parameters limit the range of energy density required to achieve a full melting. The low optical absorptivity of AlSi10Mg powder (0.19–0.32) (Gu *et al.*, 2019; Zavala-Arredondo *et al.*, 2019) and high thermal conductivity contrast between the powder and the printed material lead to variable thermal history and microstructure. As shown in Table 1, three

different batches of $8 \times 8 \times 4.5$ mm samples were produced. The energy density was remained varied between 36 and 59 J/mm^3 by adjusting the laser power and scanning speed in each batch. The manufacturer's default process parameters were considered the "near-optimal" baseline parameters from which the process parameters were varied. Batch A was built on an aluminum substrate directly without using support, while Batches B and C were produced on support structures. Each sample was only made once. However, there is overlap in terms of energy density between the samples. A study on the influence of support structure on thermal conductivity was conducted as it has not been investigated in the metal AM literature. Each batch contained vertically and horizontally aligned samples, as illustrated in Figure 1, to allow in-plane and through-plane measurement via flash diffusivity, respectively. It is worth noting, other build parameters such as shielding gas flow rate (Reijonen *et al.*, 2020), recoating speed (Phua *et al.*, 2021), particle size distribution of the powder (Bonesso *et al.*, 2021), power degradation (Raza *et al.*, 2021) and geometry of the parts (Jones *et al.*, 2021) and their location on the build plate (Mussatto *et al.*, 2022) can affect the porosity and hence the thermal performance of the fabricated part which should be investigated in the future work. Furthermore, process variation based on build design can affect residual stress (Pant *et al.*, 2020) and the thermal history, which could affect microstructure.

2.2 Sample preparation and microscopy

The samples which were directly fused onto the build platform without support structure were removed by wire electrical discharge machining. The samples printed with support structures were bandsawed from the build plate and milled to remove residual support structure.

Samples were then polished on a variable speed polisher (Buehler EcoMet 3000) using abrasives and lubricants (Allied High-Tech). The details of the polishing process are provided in the Supplementary Information.

Optical Microscopy was performed with a Zeiss Axio Imager M1m in bright field, polarized and dark-field mode. Scanning electron microscopy (SEM) in secondary electron mode, energy-dispersive X-ray spectroscopy (EDS) and electron backscatter diffraction (EBSD) was performed in a Zeiss Supra 55.

The transmission electron microscopy (TEM) characterization was done at 200 keV by FEI Talos F200X with a complementary four-quadrant energy dispersive X-ray spectroscopy (EDS) detector for elemental mapping and by JEOL JEM 2100 F microscope was used for high-resolution TEM (HRTEM), high-angle annular dark-field imaging (HAADF) and electron diffraction analyses.

2.3 Thermal properties

Thermal properties of fabricated AlSi10Mg samples with different process parameters were investigated by two main tools. Bulk thermal conductivity analysis was performed by the flash diffusivity method and local thermal conductivity measurements were performed by frequency-domain thermoreflectance.

Figure 1 (a) Schematic illustration of produced samples for thermal measurement, build axis and orientation and (b) build platform in the EOS M290 showing L-PBF AlSi10Mg samples in horizontal and vertical orientations built on support material

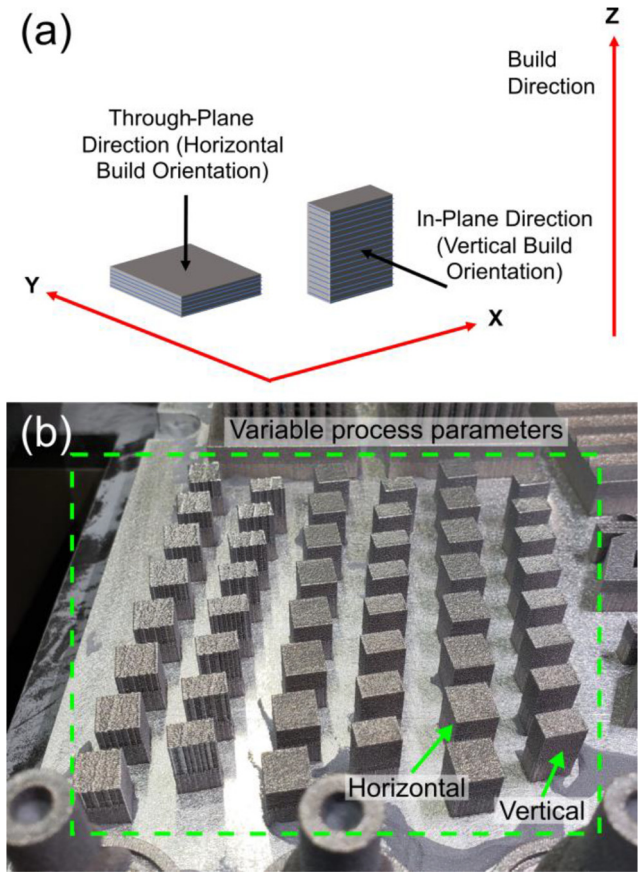

2.3.1 Flash diffusivity

The thermal diffusivities were measured using the flash diffusivity technique (Anter Flashline 2000) with samples that are $8 \times 8 \times 3.5$ mm (after polishing). The samples were coated with a thin layer of graphite to maximize flashlight absorption. The transient temperature response of the sample was fit to the Clark & Taylor model with the thermal diffusivity as a free parameter (Clark and Taylor, 1975). The thermal conductivity was calculated using the density and specific heat capacity reported in the EOS material data sheet for AlSi10Mg (EOS GmbH - Electro Optical System, 2014). Typical numerical fit to the measurements in addition to the uncertainty analysis of the flash diffusivity measurements is provided in the supplementary information.

Table 1 Processing parameters used to fabricate the L-PBF samples

Batch	No. of samples	Laser power (W)	Scanning speed (mm/s)	Support structure
A	8	370	1100–1800	No
B	13	370	1100–2400	Yes
C	9	226–370	1100	Yes

2.3.2 Frequency domain thermoreflectance

The frequency-domain thermoreflectance (FDTR) method is pump-probe technique that uses a modulated pump laser (488 nm), along with an unmodulated probe laser (532 nm) to detect the change in temperature of the sample owing to the change in reflectance with temperature (Daeumer *et al.*, 2022). To obtain a strong thermoreflectance signal a gold (Au) transducer of 200-nm film was deposited using electron-beam evaporation. The modulated pump laser frequency, f, can be kept high so that the thermal penetration depth, given by $\sqrt{\alpha/\pi f}$ where α is the thermal diffusivity, is limited to a shallow depth into the sample.

The frequency range used in this study is ~1.94–3.65 MHz to limit the thermal penetration depth to under 2.9 μm, which is helpful in detecting effects of microstructure on thermal conductivity caused by the melt pool dynamics in the L-PBF AlSi10Mg samples. The phase difference (ϕ) between the pump and the probe laser signal is used to fit experimental data to analytical solutions (Cahill, 2004, p.; Feldman, 1999). Uncertainty and sensitivity analysis of the FDTR measurements is available in the supplementary information.

2.4 Porosity and area fraction measurements

Optical microscopy measured the porosity in xz-plane of vertical samples. The optical micrographs were of a 2.5 × 2 mm area at the center of each polished sample. The images were analyzed in ImageJ software by converting them to binary mode (Schneider *et al.*, 2012).

3. Results and discussion

3.1 Densification of laser powder bed fusion parts

The size and frequency of pores is directly influenced by the laser energy density in the L-PBF process. An approximate exponential decay in porosity is observed with the increase of energy density (Figure 2). Beyond the critical value of ~40 J/mm^3, porosity approaches near zero minimum of <0.1% for AlSi10Mg. Similar trends are observed for other materials in L-PBF (e.g. stainless steel 316 L) (Simmons *et al.*, 2018, 2020). The porosity does not change significantly from 40 to 59 J/mm^3 as enough energy is provided for the material to achieve near 100% density. The lowest porosity was observed at the energy density of 59 J/mm^3 (laser scanning speed of 1100 mm/s, laser power of 370 W, layer thickness of 30 μm, hatch distance of 190 μm).Porosity starts to increase again at excessive energy densities due to increased vaporization and spatter defects (>59 J/mm^3) (Khairallah *et al.*, 2016).

3.2 Thermal properties

The experimental in-plane and though-plane thermal conductivities are shown in Figure 3. As-built samples of all batches exhibit lower in-plane than through-plane thermal conductivity (Figure 3). The thermal conductivities demonstrate an overall increasing trend with respect to energy density in both orientations. It should be noted that thermal conductivity varies due to the following:

- the porosity that forces heat to travel more circuitous routes around voids;
- the defects, interfaces and crystallinity of the Al and Si phases that lower the mean free path in these solids; and

Figure 2 Porosity in AlSi10Mg parts *vs* energy density

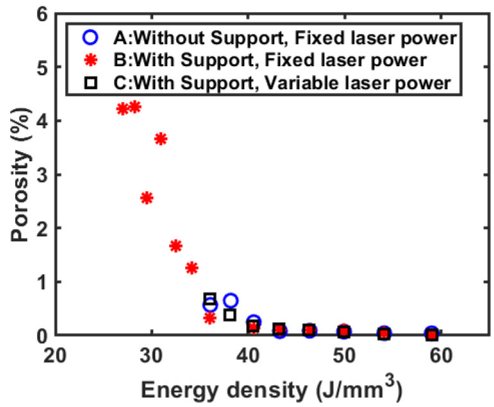

- the interfaces, especially between Al and Si phases that requires heat to convert from primarily electron-based in the Al to phonon-based in the Si (Chen, 2005; Kittel, 2004).

The effect of Si content in the Al-Si alloy on thermal properties under fixed laser process parameters was previously investigated, which showed that by the increase in Si content in the Al-Si alloy, the effective thermal conductivity decreases (Kimura *et al.*, 2017). This is due to Si solute acting as scattering sites for electrons which increases thermal resistivity. Earlier studies demonstrated for other materials that too low of an energy density results in poor fusion between the layers due to a shallower melt pool (Aboulkhair *et al.*, 2014; Calignano *et al.*, 2018; Damon *et al.*, 2018; Zavala-Arredondo *et al.*, 2019). On the other hand, excessive powers lead to melt pool instability and keyhole voids, as well as spatter at even higher energy densities (Gibson *et al.*, 2015).

The data shows the thermal conductivity of as-built AlSi10Mg without support (batch A; open blue circles) is higher than those manufactured on support (batch B and C; red asterisks and open black squares) at higher energy densities (>50 J/mm^3). A larger heat buildup was observed in the L-PBF parts built on support structure compared with the parts fabricated directly on the build plate (Song *et al.*, 2019). Owing to the poorer thermal conductivity of support material compared to solid metal, the support has slower cooling rates in subsequent layers and higher overall temperatures, impacting microstructure (Hu *et al.*, 2016). While not explored in this work, printing unsupported overhang would pose similar low-thermal conductivity support scenarios, and change thermal conductivity of subsequent build layers. For design considerations, in the applications that require higher as-built thermal conductivity, it can be recommended to print the part directly onto the build plate. It is worth mentioning the maximum of the thermal conductivity values for the in-plane and through-plane cases were at different energy densities (50 J/mm^3 vs 59 J/mm^3). Beside the porosity effect which will be discussed next, this may be due to spatial thermal gradients that impacts in-plane more than through-plane thermal conductivity.

Figure 4 indicates that the high porosity of samples fabricated using an energy density of 27–40 J/mm^3 reduces thermal conductivity in all directions due to a combination of porosity and microstructural changes. Maxwell-Garnett approximation was used to calculate the upper limit of thermal conductivity as a function of porosity based on the effective medium model

Figure 3 In-plane (a) and through-plane (b) thermal conductivity versus energy density for L-PBF AlSi10Mg

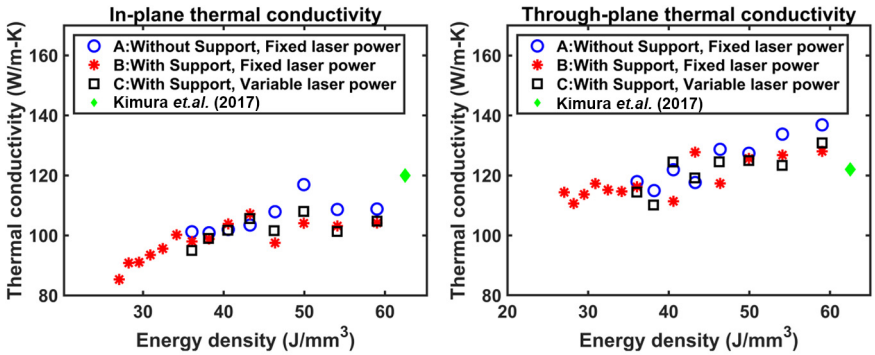

Note: The flash diffusivity data has an absolute uncertainty of 7 W/m-K and a relative uncertainty of 2 W/m-K (Supplementary Information section 1)

(Markel, 2016). The thermal conductivity value was expected to reach the theoretical limit for low porosity samples. However, measurements revealed lower thermal conductivity value for some samples in the low porosity region. It is hypothesized that the variation in thermal conductivity of low porosity samples (40–59 J/mm^3) derives primarily from their microstructure rather than their porosity, which will be explained in detail in our microscopy and thermal mapping analysis. It is also noteworthy that our highest measured through-plane thermal conductivity of 136 ± 2 W/m-K (laser energy density of 59 J/mm^3, without support structure, laser scanning speed of 1100 mm/s, laser power of 370 W, layer thickness of 30 μm, hatch distance of 190 μm), is greater than any previously as-built L-PBF AlSi10Mg, with the next highest being 120 W/m-K at room temperature (Silbernagel *et al.*, 2018).

3.3 Microstructure evolution

The optical micrographs of the xy-plane and xz-plane are shown in Figure 5. The laser raster direction rotated 67° clockwise every layer (EOS process parameter terms laser raster direction), which is visible from the build-plane xy view [Figure 5(a)]. Also visible are melt pool instabilities causing the width of melt pools in the top and cross section views to be variable [Figure 5(b)]. In the cross-section sample xz view, several melt pools are elongated as those melt pools aligned with the raster direction [Figure 5(a)] (Padovano *et al.*, 2020).

Scanning electron microscopy reveals three regions in the microstructure:

1 the melt pool (MP);
2 the coarse-grained zone (CGZ); and
3 the heat affected zone (HAZ).

The MP is most important volume in terms of thermal conductivity of the bulk, as it encompasses most of the printed volume. The combination of xy- and xz-plane SEM images reveal the MP volumes contain columnar dendritic grains that have a tendency to align about the z-direction, while the same regions appears cellular when viewed from the xy-plane (Hadadzadeh *et al.*, 2018). This vertical orientation has implications to anisotropic conductivity that will be discussed

Figure 4 Thermal conductivity versus porosity of L-PBF parts

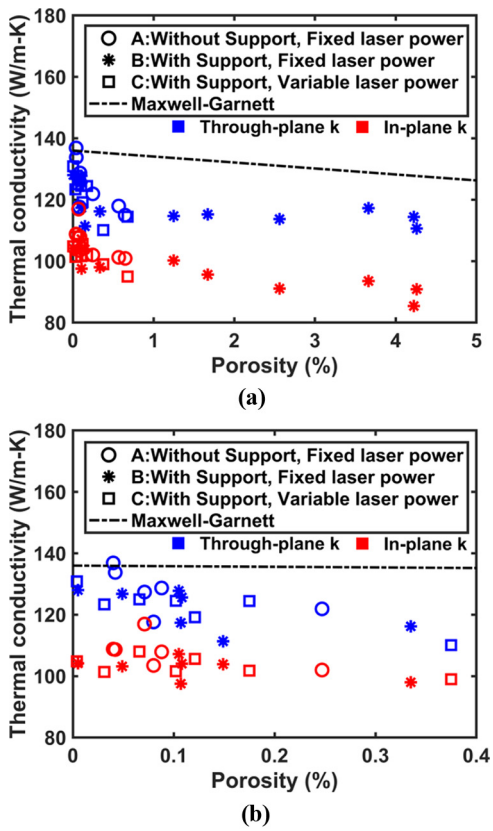

Notes: (a) Entire sample set; (b) samples with porosities under 0.4%. The flash diffusivity data has an absolute uncertainty of 7 W/m-K and a relative uncertainty of 2 W/m-K (Supplementary Information section 1)

subsequently. The secondary electron microscopy images indicate the Si-rich phase as white, and α-Al phase as dark gray. The coarse grain zone has the highest thermal gradient during solidification in the melt pool, resulting in the formation of a coarse, (Liu *et al.*, 2019a; Mertens *et al.*, 2020;

Figure 5 Microstructure of L-PBF AlSi10Mg

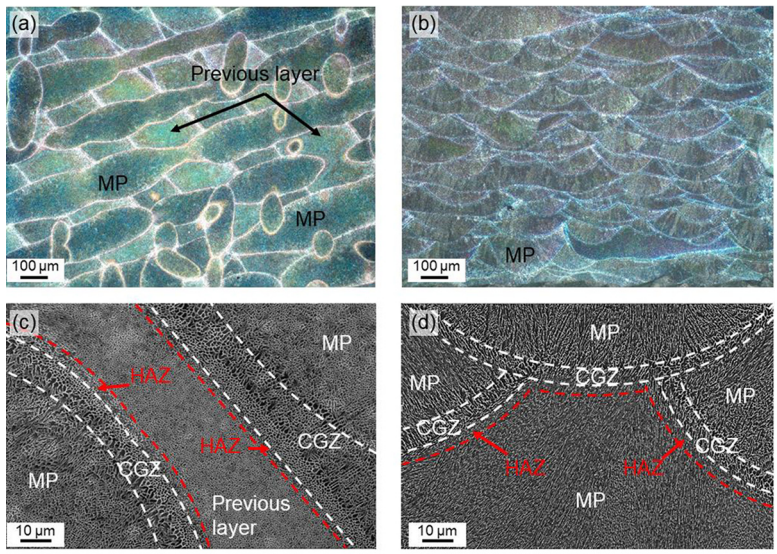

Notes: Optical micrographs of (a) xy-plane; (b) xz-plane; details of solidification morphology in SEM images; (c) xy-plane; (d) xz-plane

Figure 6 Microstructure of L-PBF samples from batch A fabricated using energy densities of 40 J/mm^3 (panels a, c, e) and 59 J/mm^3 (panels b, d, f)

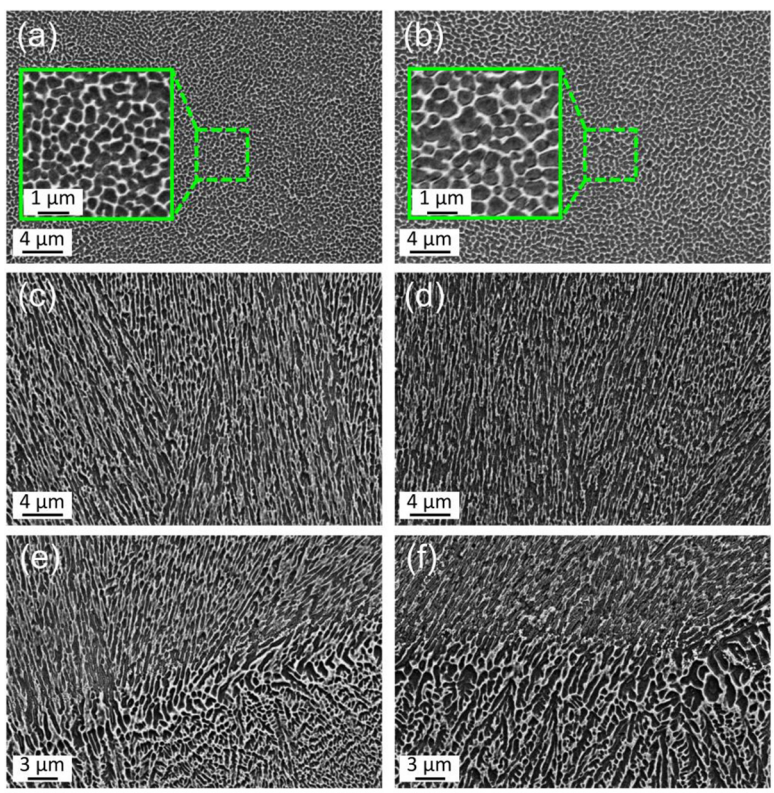

Notes: (a); (b) melt pool center at xy-plane; (c); (d) melt pool center at xz-plane; (e);(f) melt pool boundary at xz-plane of the samples with 40 and 59 J/mm^3, respectively

Thijs *et al.*, 2013) and brittle microstructure (Maconachie *et al.*, 2020). The heat affected zone is adjacent to the melt pool boundary and contains a broken Si network structure due to successive reheating by subsequent thermal cycles (Fathi *et al.*, 2019).

During the L-PBF process, α-Al phase precipitates from the liquid first which segregates the Si (Wang *et al.*, 2018). The SEM images of Figures 5 and 6 reveal the thick Si-rich areas. Our subsequent TEM images reveal the fractal nature of this segregation that occurs inside the α-Al regions as well (Figures 7 and 8). Figure 6 compares the crystal grain size of samples produced with 40 J/mm^3 (panels a, c, e) versus those produced at 59 J/mm^3 energy density (panels b, d, f). Overall, the 40 J/mm^3 energy density grains possess a finer substructure than 59 J/mm^3 grains, due to faster quenching and less subsequent rewarming at lower energy densities (Hu *et al.*, 2016). This has implications to the trends of thermal conductivity vs energy density, as heat will have fewer interfaces to pass at higher energy densities.

Transmission electron microscopy was performed on two samples with the laser energy density of 59 J/mm^3 (1100 mm/s, 370 W) and 40 J/mm^3 (1600 mm/s, 370 W). Higher and lower energy density samples were focused ion beamed to show the xz-plane (Figure 7) and xy-plane (Figure 8) microstructures, respectively.

Al-Si columnar dendritic and cellular structures are observed in the TEM images based on the orientation of the grains. Long anisotropic columns of Al in the xz-plane orientation (Figure 7) are attributed to contribute to higher thermal conductivity in the xz-plane direction as a result of more efficient transport mechanism in the Al due to less concentration of electron and phonon scattering sites by Si. Electron diffraction pattern and high-resolution transmission electron microscopy (HRTEM) images confirm Al in the columnar dendritic structure is single crystal. However, Si is mostly polycrystalline which possess lower thermal conductivity.

In the xy-plane view TEM, the microstructure shows Al cores and Si shells in cellular structure. It is observed that the interdendrite Si phase is single crystalline in the imaged location (although polycrystalline in other locations) but highly defective, composed of stacking faults, twin planes, and nano-twins [Figure 8(j-l)]. Formation of defective Si phase is attributed to be due to the rapid solidification during the L-PBF process, lowering conductivity far below ideal single crystal level (McConnell *et al.*, 2001). The TEM image of the xy-plane appears cellular, while the TEM of the xz plane

Figure 7 TEM characterizations of the columnar crystals with energy density of 59 J/mm^3 (1100 mm/s, 370 W)

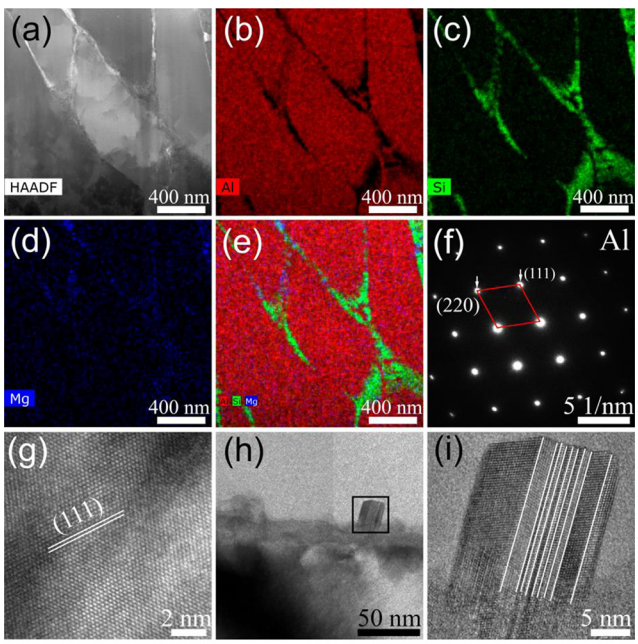

Notes: (a-e) Low-magnification HAADF-STEM image and the corresponding EDS mapping of the 3-D printed AlSi10Mg sample showing the crystal morphology and the elemental distribution cross the as-synthesized sample. The overlay EDS map of Al (red), Si (green) and Mg (blue) in I presents the elemental enrichment of Si and Mg at the grain boundaries. (f, g) The corresponding diffraction pattern and the HRTEM image of the Al substrate, as marked by the solid white rectangle in (e). (h) The low magnification TEM images displaying the segregation induced Si precipitate formation at grain boundaries, and the corresponding high magnification TEM view in (i). The white lines mark the nano-twin planes of the Si precipitate in (i)

Figure 8 TEM characterizations of the isometric crystal with energy density of 40 J/mm^3 (1600 mm/s, 370 W)

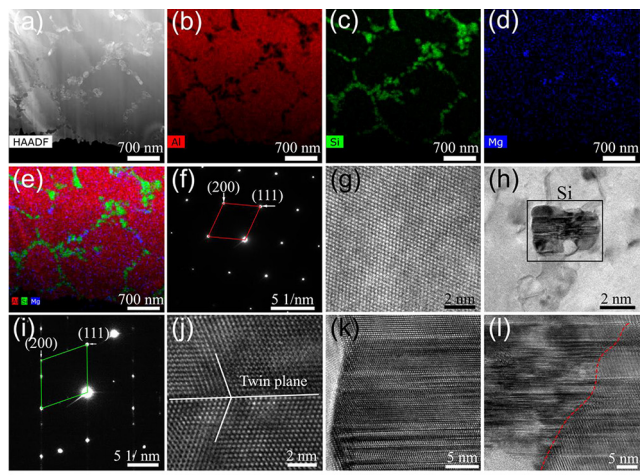

Notes: Low-magnification HAADF-scanning transmission electron microscopy (STEM) image and the corresponding EDS maps of the isometric crystal illustrating the crystal morphology and compositional distribution of the as-builtbuilt sample. The EDS overlay maps of Al (red), Si (green), and Mg (blue) in (b-d) show the elemental enrichment of Si and Mg at the grain boundaries in (e). (f, g) The diffraction pattern and the HRTEM image of Al, as marked by the solid white square in (e). (h, i) The low magnification TEM image of the segregated Si precipitate and the corresponding diffraction pattern. (j-l) The enlarged views of the Si precipitate displaying the defective Si precipitate, including the well-established twin boundary, nano-twin planes and the high-density stacking faults. The dashed red line in (l) highlights the domain boundary

appears columnar. This is consistent with what was observed for xy- and xz- SEM images earlier. This indicates the grains have a fractal-like columnar microstructure with the long axis oriented in the z-direction, such that xy-slices generally appear cellular. The large inter-colony Si deposits show up more clearly in SEM, but it is believed that the finer more frequent Si inter-granular deposits lead to greater thermal impact owing to their much greater number of interfaces.

3.4 Thermal analysis

Our co-located EBSD and thermal conductivity map taken with mapping FDTR show that longer grain colonies have higher thermal conductivity than finer grains (Figure 9). This is due to longer grain colonies also having a coarser grain structure that has fewer Al-Si interfaces to impede thermal transport.

Figure 9 (a) EBSD image of AlSi10Mg sample with energy density of 40 J/mm^3 of the xz-plane; (b) zoomed-in EBSD map showing larger and finer colonies of columnar grains separated by a melt pool boundary and (c) FDTR mapping on the same location as the zoomed-in EBSD image showing larger colonies of columnar grains having higher thermal conductivity compared to smaller columnar grains due to fewer silicon interfaces, especially at the intergrain level

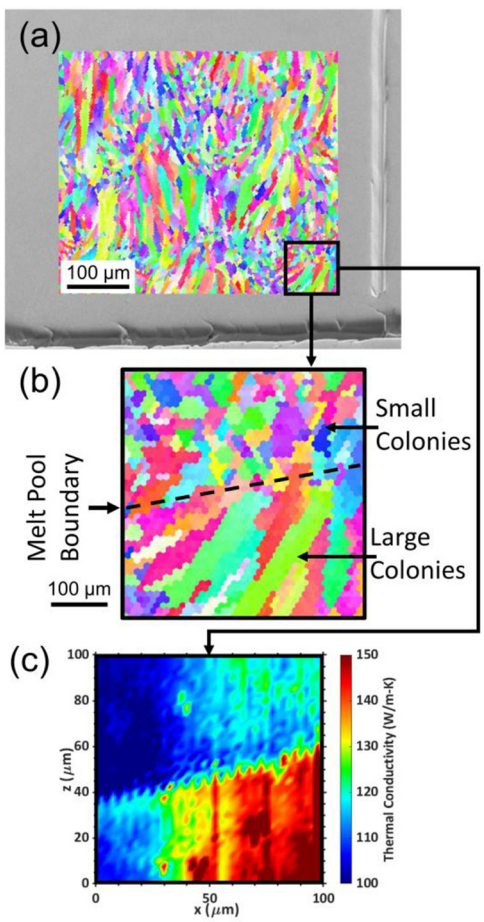

Note: The thermal conductivity map has an absolute uncertainty of 9 W/m-K and a relative uncertainty of 2 W/m-K between pixels (Supplementary Information section 3)

The Si has lower thermal conductivity than pure single crystal Al (237 W/m-K) (Sélo *et al.*, 2020). While pristine single crystal Si has a thermal conductivity of ~140 W/m-K, Si can have significantly lower thermal conductivity when it is multi-crystalline, defective, doped or extremely thin in one dimension. The thermal conductivity of the aluminum alloy will also change with purity of the alloy, as the alloying elements scatter electrons. The thermal transport through this composite requires the heat to convert from electrons to phonons as heat passes from the metal to the Si boundaries, impeding thermal transport. The through-plane direction contains elongated cells with α-Al matrix relative to the in-plane direction on average. This microstructural difference results in fewer interfacial boundaries in the through-plane relative to the in-plane directions; hence, through-plane (z-direction) is greater than in-plane conductivity (xy-directions).

The effective composite thermal conductivity can be estimated using the following model that accounts for the thermal resistance due to the volume of aluminum, silicon and frequency of interfaces:

$$\frac{1}{k_e} = \frac{x_{Al}}{k_{Al}} + \frac{1 - x_{Al}}{k_{Si}} + \frac{2}{L_c h_{Al-Si}} \quad (1)$$

Equation (1) where k_e is the effective composite thermal conductivity, x_{Al} is the volume fraction of Al, k_{Al} is the thermal conductivity of the Al phase, k_{Si} is the thermal conductivity of the Si phase, L_c is the characteristic grain size and $h_{Al\text{-}Si}$ is the interfacial conductance of the interface between Al and Si (detailed explanation in Supplementary Information Section 5). Experimental measurements of Al-Si interfaces found that the interfacial resistance varied between 350 and 220 MW/m^2-K for atomically smooth Si. Even lower values of 200–150 MW/m^2-K for roughened Si-Al interfaces were reported (Hopkins *et al.*, 2011). This Al-Si interfacial conductance has contributions due to disorder/mixing near the interface, electron-phonon coupling in the Al and conductance of phonons from the Al to Si (Hopkins *et al.*, 2011; Majumdar and Reddy, 2004; Yang *et al.*, 2015). Figure 10 shows the effective thermal

Figure 10 The predicted composite thermal conductivity versus characteristic grain size for interfacial Al-Si conductance based on literature measurements (Hopkins *et al.*, 2011; Majumdar and Reddy, 2004; Yang *et al.*, 2015) that ranged from 350 to 150 MW/m^2-K; the upper and lower limit measured are indicated by dashed horizontal lines

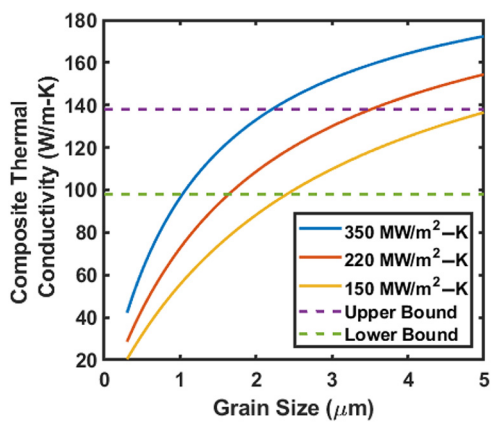

conductivity versus characteristic grain size for interfacial conductances within the range measured for pure Si-Al systems. Thermal conductivity can be seen to vary sharply with grain size. This modeling combined with our TEM and SEM provides strong evidence that electron-phonon interfaces dominate the thermal properties of this alloy system. This refutes the hypothesis found in some literature that phonon scattering at grain boundaries is the dominant factor in thermal conductivity (Elkholy *et al.*, 2022).

4. Conclusion

An anisotropy is observed in the thermal conductivity value of optimally printed as-built through-plane (136 ± 2 W/m-K) and in-plane (117 ± 2 W/m-K) L-PBF-AlSi10Mg samples. Furthermore, the thermal conductivity in in-plane and through-plane samples depend on the energy density and support material. Changes in porosity with processing do not explain the bulk of the thermal conductivity changes with near-optimal energy density. However, microstructural variations in the segregated Al-Si phase do explain the observed thermal conductivity trend. Si acts as phonon and electron scattering sites which impedes thermal transport in Al. Co-located grain orientation mapping by EBSD and thermal conductivity mapping by FDTR revealed regions with longer colonies of columnar grains possess higher thermal conductivity owing to fewer silicon-aluminum interfaces. The trends in thermal conductivity have important applications to AlSi10Mg for thermal-related applications, simulations of thermal stresses and laser processing in L-PBF and thermal-based on non-destructive testing. It is worth noting, other parameters affecting thermal properties of the L-PBF parts including powder degradation, shielding gas, particle size distribution and geometry should be investigated in future research.

Acknowledgement

The authors gratefully acknowledge awards from the US Department of Commerce, National Institute of Standards and Technology (NIST) 70NANB22H085, and the National Science Foundation (NSF) 1941181 and 1846157. The authors thank Dr. Junghyun Cho for use of various sample preparation tools. Xiaobo Chen and Guangwen Zhou acknowledge the support by the National Science Foundation (NSF) under the NSF Collaborative Research Award grant DMR 1905422. This research used resources of the Center for Functional Nanomaterials (CFN), which is a US Department of Energy Office of Science User Facility, at Brookhaven National Laboratory under Contract No. DE-SC0012704.

Author contributions: Scott N Schiffres conceived the initial idea of this research and contributed to advising the work. Guangwen Zhou also contributed to advising the work, especially relating to the analysis of samples with TEM. Arad Azizi designed and developed the processing technique, and performed sample fabrications, post-processing, SEM characterizations, EBSD and analyses. Fatemeh Hejripour helped with metallurgical and thermal analyses. Jacob A Goodman performed flash diffusivity testing and analysis and performed sample preparations and polishing. Piyush A Kulkarni performed the experimental thermal conductivity map measurements using FDTR method. Xiaobo Chen performed FIB and analyzed the sample with TEM. All authors contributed to the writing of this paper.

Declaration of competing interest: Several of the authors have a prior patent application related to thermal nondestructive testing.

References

Aboulkhair, N.T., Everitt, N.M., Ashcroft, I. and Tuck, C. (2014), "Reducing porosity in AlSi10Mg parts processed by selective laser melting", *Additive Manufacturing*, Vol. 1, pp. 77-86.

Aboulkhair, N.T., Simonelli, M., Parry, L., Ashcroft, I., Tuck, C. and Hague, R. (2019), "3D printing of aluminium alloys: additive manufacturing of aluminium alloys using selective laser melting", *Progress in Materials Science*, Vol. 106, p. 100578.

Alexandersen, J., Sigmund, O., Meyer, K.E. and Lazarov, B.S. (2018), "Design of passive coolers for light-emitting diode lamps using topology optimisation", *International Journal of Heat and Mass Transfer*, Vol. 122, pp. 138-149.

Alihosseini, Y., Zabetian Targhi, M., Heyhat, M.M. and Ghorbani, N. (2020), "Effect of a micro heat sink geometric design on thermo-hydraulic performance: a review", *Applied Thermal Engineering*, Vol. 170, p. 114974, doi: 10.1016/j.applthermaleng.2020.114974.

Azizi, A. and Schiffres, S.N. (2018), "Laser metal additive manufacturing on graphite", *Proceedings of the 29th Annual International Solid Freeform Fabrication Symposium – An Additive Manufacturing Conference, Reviewed Paper, Presented at the Solid Freeform Fabrication, Austin, TX, USA*, pp. 2315-2324.

Azizi, A., Chen, X., Gou, F., Hejripour, F., Goodman, J.A., Bae, I.-T., Rangarajan, S., *et al.* (2022), "Selective laser melting of metal structures onto graphite substrates via a low melting point interlayer alloy", *Applied Materials Today*, Vol. 26, p. 101334.

Azizi, A., Daeumer, M.A. and Schiffres, S.N. (2019a), "Additive laser metal deposition onto silicon", *Additive Manufacturing*, Vol. 25, pp. 390-398.

Azizi, A., Daeumer, M.A., Simmons, J.C., Sammakia, B.G., Murray, B.T. and Schiffres, S.N. (2019b), "Additive Laser metal deposition onto silicon for enhanced microelectronics cooling", *2019 IEEE 69th Electronic Components and Technology Conference (ECTC), IEEE, Las Vegas, NV, USA*, pp. 1970-1976.

Bagherifard, S., Beretta, N., Monti, S., Riccio, M., Bandini, M. and Guagliano, M. (2018), "On the fatigue strength enhancement of additive manufactured AlSi10Mg parts by mechanical and thermal post-processing", *Materials and Design*, Vol. 145, pp. 28-41.

Bonesso, M., Rebesan, P., Gennari, C., Mancin, S., Dima, R., Pepato, A. and Calliari, I. (2021), "Effect of particle size distribution on laser powder bed fusion manufacturability of copper", *BHM Berg – Und Hüttenmännische Monatshefte*, Vol. 166 No. 5, pp. 256-262.

Butler, C., Babu, S., Lundy, R., O'Reilly Meehan, R., Punch, J. and Jeffers, N. (2021), "Effects of processing parameters and heat treatment on thermal conductivity of additively manufactured AlSi10Mg by selective laser melting", *Materials Characterization*, Vol. 173, p. 110945.

Cahill, D.G. (2004), "Analysis of heat flow in layered structures for time-domain thermoreflectance", *Review of Scientific Instruments*, Vol. 75 No. 12, pp. 5119-5122.

Calignano, F., Cattano, G. and Manfredi, D. (2018), "Manufacturing of thin wall structures in AlSi10Mg alloy by laser powder bed fusion through process parameters", *Journal of Materials Processing Technology*, Vol. 255, pp. 773-783.

Chen, G. (2005), *Nanoscale Energy Transport and Conversion: A Parallel Treatment of Electrons, Molecules, Phonons, and Photons*, Oxford University Press, available at: https://books.google.com/books?id=M3n3lUJpYDYC&lpg=PR7&ots=kx2ygpTb_q&dq=gang%20chen%202005&lr&pg=PR7#v=onepage&q=gang%20chen%202005&f=false

Chen, J.K., Hung, H.Y., Wang, C.F. and Tang, N.K. (2017), "Effects of casting and heat treatment processes on the thermal conductivity of an Al-Si-Cu-Fe-Zn alloy", *International Journal of Heat and Mass Transfer*, Vol. 105, pp. 189-195.

Clark, L.M., III. and Taylor, R.E. (1975), "Radiation loss in the flash method for thermal diffusivity", *Journal of Applied Physics*, Vol. 46 No. 2, pp. 714-719.

Collins, I.L., Weibel, J.A., Pan, L. and Garimella, S.V. (2019), "A permeable-membrane microchannel heat sink made by additive manufacturing", *International Journal of Heat and Mass Transfer*, Vol. 131, pp. 1174-1183.

Daeumer, M., Sandoval, E.D., Azizi, A., Bagheri, M.H., Bae, I.T., Panta, S., Koulakova, E.A., Cotts, E., Arvin, C.L., Kolmogorov, A.N. and Schiffres, S.N. (2022), "Orientation-Dependent transport properties of Cu3Sn", *Acta Materialia*, Vol. 227, p. 117671.

Damon, J., Dietrich, S., Vollert, F., Gibmeier, J. and Schulze, V. (2018), "Process dependent porosity and the influence of shot peening on porosity morphology regarding selective laser melted AlSi10Mg parts", *Additive Manufacturing*, Vol. 20, pp. 77-89.

Di Sabatino, M. and Arnberg, L. (2009), "Castability of aluminium alloys", *Transactions of the Indian Institute of Metals*, Vol. 62, pp. 321-325.

Dokken, C.B. and Fronk, B.M. (2018), "Optimization of 3D printed liquid cooled heat sink designs using a micro-genetic algorithm with bit array representation", *Applied Thermal Engineering*, Vol. 143, pp. 316-325.

Elkholy, A., Quinn, P., Uí Mhurchadha, S.M., Raghavendra, R. and Kempers, R. (2022), "Characterization and analysis of the thermal conductivity of AlSi10Mg fabricated by laser powder bed fusion", *Journal of Manufacturing Science and Engineering*, Vol. 144 No. 10, p. 101001.

EOS GmbH – Electro Optical System (2014), "EOS Aluminium AlSi10Mg material data sheet", available at: https://fathommfg.com/wp-content/uploads/2020/11/EOS_Aluminium_AlSi10Mg_en.pdf (accessed 8 August 2022).

Fasano, M., Ventola, L., Calignano, F., Manfredi, D., Ambrosio, E.P., Chiavazzo, E. and Asinari, P. (2016), "Passive heat transfer enhancement by 3D printed pitot tube based heat sink", *International Communications in Heat and Mass Transfer*, Vol. 74, pp. 36-39.

Fathi, P., Rafieazad, M., Duan, X., Mohammadi, M. and Nasiri, A.M. (2019), "On microstructure and corrosion behaviour of AlSi10Mg alloy with low surface roughness fabricated by direct metal laser sintering", *Corrosion Science*, Vol. 157, pp. 126-145.

Feldman, A. (1999), "Algorithm for solutions of the thermal diffusion equation in a stratified medium with a modulated heating source", *High Temp-High Pressures*, Vol. 31 No. 3, pp. 293-298.

Fulcher, B.A., Leigh, D.K. and Watt, T.J. (2014), "Comparison of ALSI10MG and AL 6061 processed through DMLS", *25th Annual International Solid Freeform Fabrication Symposium &#65533; An Additive Manufacturing Conference, SFF 2014*, pp. 404-419.

Gibson, I., Rosen, D. and Stucker, B. (2015), *Additive Manufacturing Technologies*, Springer, New York, NY, doi: 10.1007/978-1-4939-2113-3.

Gu, D., Yang, Y., Xi, L., Yang, J. and Xia, M. (2019), "Laser absorption behavior of randomly packed powder-bed during selective laser melting of SiC and TiB2 reinforced Al matrix composites", *Optics and Laser Technology*, Vol. 119, p. 105600.

Hadadzadeh, A., Amirkhiz, B.S., Li, J. and Mohammadi, M. (2018), "Columnar to equiaxed transition during direct metal laser sintering of AlSi10Mg alloy: effect of building direction", *Additive Manufacturing*, Vol. 23, pp. 121-131.

Hopkins, P.E., Phinney, L.M., Serrano, J.R. and Beechem, T. E. (2011), "Effects of surface roughness and oxide layer on the thermal boundary conductance at aluminum/silicon interfaces", *American Society of Mechanical Engineers Digital Collection*, Vol. 49415, pp. 313-319.

Hu, H., Ding, X. and Wang, L. (2016), "Numerical analysis of heat transfer during multi-layer selective laser melting of AlSi10Mg", *Optik*, Vol. 127 No. 20, pp. 8883-8891.

Jawade, S.A., Joshi, R.S. and Desai, S.B. (2020), "Comparative study of mechanical properties of additively manufactured aluminum alloy", *Materials Today: Proceedings*, Vol. 46, pp. 9270-9274, doi: 10.1016/j.matpr.2020.02.096.

Jones, A., Leary, M., Bateman, S. and Easton, M. (2021), "Effect of surface geometry on laser powder bed fusion defects", *Journal of Materials Processing Technology*, Vol. 296, p. 117179.

Kempen, K., Thijs, L., Van Humbeeck, J. and Kruth, J.P. (2012), "Mechanical Properties of AlSi10Mg produced by selective laser melting", *Physics Procedia*, Vol. 39, pp. 439-446.

Khairallah, S.A., Anderson, A.T., Rubenchik, A. and King, W. E. (2016), "Laser powder-bed fusion additive manufacturing: physics of complex melt flow and formation mechanisms of pores, spatter, and denudation zones", *Acta Materialia*, Vol. 108, pp. 36-45.

Kim, M.-S. (2021), "Effects of processing parameters of selective laser melting process on thermal conductivity of AlSi10Mg alloy", *Materials*, Vol. 14 No. 9, p. 2410.

Kimura, T., Nakamoto, T., Mizuno, M. and Araki, H. (2017), "Effect of silicon content on densification, mechanical and thermal properties of Al-xSi binary alloys fabricated using

selective laser melting", *Materials Science and Engineering A*, Vol. 682, pp. 593-602.

Kirsch, K.L. and Thole, K.A. (2017), "Pressure loss and heat transfer performance for additively and conventionally manufactured pin fin arrays", *International Journal of Heat and Mass Transfer*, Vol. 108, pp. 2502-2513.

Kittel, C. (2004), *Introduction to Solid State Physics*, 8th ed., Wiley, available at: www.wiley.com/en-us/Introduction+to+Solid+State+Physics%2C+8th+Edition-p-9780471415268

Liu, B., Li, B.Q. and Li, Z. (2019a), "Selective laser remelting of an additive layer manufacturing process on AlSi10Mg", *Results in Physics*, Vol. 12, pp. 982-988.

Liu, G., Xiong, J. and Tang, L. (2020), "Microstructure and mechanical properties of 2219 aluminum alloy fabricated by double-electrode gas metal arc additive manufacturing", *Additive Manufacturing*, Vol. 35, p. 101375.

Liu, X., Zhao, C., Zhou, X., Shen, Z. and Liu, W. (2019b), "Microstructure of selective laser melted AlSi10Mg alloy", *Materials & Design*, Vol. 168, p. 107677.

Lu, T.J., Stone, H.A. and Ashby, M.F. (1998), "Heat transfer in open-cell metal foams", *Acta Materialia*, Vol. 46 No. 10, pp. 3619-3635.

Maamoun, A.H., Xue, Y.F., Elbestawi, M.A. and Veldhuis, S. C. (2018), "The effect of selective laser melting process parameters on the microstructure and mechanical properties of Al6061 and AlSi10Mg alloys", *Materials*, Vol. 12 No. 1, p. 2343.

McConnell, A.D., Uma, S. and Goodson, K.E. (2001), "Thermal conductivity of doped polysilicon layers", *Journal of Microelectromechanical Systems*, Vol. 10 No. 3, pp. 360-369.

Maconachie, T., Leary, M., Zhang, J., Medvedev, A., Sarker, A., Ruan, D., Lu, G., *et al.* (2020), "Effect of build orientation on the quasi-static and dynamic response of SLM AlSi10Mg", *Materials Science and Engineering A*, Vol. 788, p. 139445, doi: 10.1016/j.msea.2020.139445.

Majumdar, A. and Reddy, P. (2004), "Role of electron–phonon coupling in thermal conductance of metal–nonmetal interfaces", *Applied Physics Letters*, Vol. 84 No. 23, pp. 4768-4770.

Markel, V.A. (2016), "Introduction to the Maxwell Garnett approximation: tutorial", *Journal of the Optical Society of America A*, Vol. 33 No. 7, p. 1244.

Mathers, G. (2002), *The Welding of Aluminium and Its Alloys*, Woodhead Publishing, available at: www.sciencedirect.com/book/9781855735675/the-welding-of-aluminium-and-its-alloys#book-info

Meier, C., Penny, R.W., Zou, Y., Gibbs, J.S. and Hart, A.J. (2018), "Thermophysical Phenomena in metal additive manufacturing by selective laser melting: fundamentals, modeling, simulation, and experimentation", *Annual Review of Heat Transfer*, Vol. 20 No. 1, pp. 241-316.

Mertens, A., Delahaye, J., Dedry, O., Vertruyen, B., Tchuindjang, J.T. and Habraken, A.M. (2020), "Microstructure and properties of SLM AlSi10Mg: understanding the influence of the local thermal history", *Procedia Manufacturing*, Vol. 47, pp. 1089-1095.

Moon, H., Miljkovic, N. and King, W.P. (2020), "High power density thermal energy storage using additively manufactured heat exchangers and phase change material", *International Journal of Heat and Mass Transfer*, Vol. 153, p. 119591, doi: 10.1016/j.ijheatmasstransfer.2020.119591.

Mussatto, A., Groarke, R., Vijayaraghavan, R.K., Hughes, C., Obeidi, M.A., Doğu, M.N., Yalçin, M.A., McNally, P.J., Delaure, Y. and Brabazon, D. (2022), "Assessing dependency of part properties on the printing location in laser-powder bed fusion metal additive manufacturing", *Materials Today Communications*, Vol. 30, p. 103209.

Padovano, E., Badini, C., Pantarelli, A., Gili, F. and D'Aiuto, F. (2020), "A comparative study of the effects of thermal treatments on AlSi10Mg produced by laser powder bed fusion", *Journal of Alloys and Compounds*, Vol. 831, p. 154822, doi: 10.1016/j.jallcom.2020.154822.

Pant, P., Proper, S., Luzin, V., Sjöström, S., Simonsson, K., Moverare, J., Hosseini, S., *et al.* (2020), "Mapping of residual stresses in as-built inconel 718 fabricated by laser powder bed fusion: a neutron diffraction study of build orientation influence on residual stresses", *Additive Manufacturing*, Vol. 36, p. 101501.

Phua, A., Doblin, C., Owen, P., Davies, C.H.J. and Delaney, G.W. (2021), "The effect of recoater geometry and speed on granular convection and size segregation in powder bed fusion", *Powder Technology*, Vol. 394, pp. 632-644.

Raus, A.A., Wahab, M.S., Ibrahim, M., Kamarudin, K., Ahmed, A. and Shamsudin, S. (2017), "Mechanical and physical properties of AlSi10Mg processed through selective laser melting", *AIP Conference Proceedings*, Vol. 1831, p. 20027, doi: 10.1063/1.4981168.

Raza, A., Fiegl, T., Hanif, I., MarkstrÖm, A., Franke, M., Körner, C. and Hryha, E. (2021), "Degradation of AlSi10Mg powder during laser based powder bed fusion processing", *Materials & Design*, Vol. 198, p. 109358.

Read, N., Wang, W., Essa, K. and Attallah, M.M. (2015), "Selective laser melting of AlSi10Mg alloy: process optimisation and mechanical properties development", *Materials and Design*, Vol. 65, pp. 417-424.

Reijonen, J., Revuelta, A., Riipinen, T., Ruusuvuori, K. and Puukko, P. (2020), "On the effect of shielding gas flow on porosity and melt Pool geometry in laser powder bed fusion additive manufacturing", *Additive Manufacturing*, Vol. 32, p. 101030.

Schiffres, S.N. and Azizi, A. (2021), "Additive manufacturing processes and additively manufactured products", 9 November, available at: https://patents.google.com/patent/US11167375B2/en (accessed 10 December 2021).

Schiffres, S.N., Daeumer, M.A., Simmons, J.C. and Azizi, A. (2020), "Enhanced non-destructive testing in directed energy material processing".

Schneider, C.A., Rasband, W.S. and Eliceiri, K.W. (2012), "NIH Image to ImageJ: 25 years of image analysis", *Nature methods*, Vol. 9 No. 7, pp. 671-675.

Sélo, R.R.J., Catchpole-Smith, S., Maskery, I., Ashcroft, I. and Tuck, C. (2020), "On the thermal conductivity of AlSi10Mg and lattice structures made by laser powder bed fusion", Additive *Manufacturing*, Vol. 34, p. 101214.

Shin, J., Ko, S. and Kim, K. (2014), "Development of low-Si aluminum casting alloys with an improved thermal conductivity", *Materiali in Tehnologije*, Vol. 48 No. 2, pp. 195-202.

Silbernagel, C., Ashcroft, I., Dickens, P. and Galea, M. (2018), "Electrical resistivity of additively manufactured AlSi10Mg for use in electric motors", *Additive Manufacturing*, Vol. 21, pp. 395-403.

Simmons, J.C., Chen, X., Azizi, A., Daeumer, M.A., Zavalij, P.Y., Zhou, G. and Schiffres, S.N. (2020), "Influence of processing and microstructure on the local and bulk thermal conductivity of selective laser melted 316L stainless steel", *Additive Manufacturing*, Vol. 32, p. 100996, doi: 10.1016/j.addma.2019.100996.

Simmons, J., Daeumer, M., Azizi, A. and Schiffres, S.N. (2018), "Local thermal conductivity mapping of selective laser melted 316L stainless steel", *Proceedings of the 29th Annual International Solid Freeform Fabrication Symposium – An Additive Manufacturing Conference., presented at the Solid Freeform Fabrication 2018, Austin, TX, USA*, pp. 1694-1707.

Song, H., Mcgaughy, T., Sadek, A. and Zhang, W. (2019), "Effect of structural support on microstructure of nickel base superalloy fabricated by laser-powder bed fusion additive manufacturing", *Additive Manufacturing*, Vol. 26, pp. 30-40.

T'Joen, C., De Jaeger, P., Huisseune, H., Van Herzeele, S., Vorst, N. and De Paepe, M. (2010), "Thermo-hydraulic study of a single row heat exchanger consisting of metal foam covered round tubes", *International Journal of Heat and Mass Transfer*, Vol. 53 Nos 15/16, pp. 3262-3274.

Thijs, L., Kempen, K., Kruth, J.P. and Van Humbeeck, J. (2013), "Fine-structured aluminium products with controllable texture by selective laser melting of pre-alloyed AlSi10Mg powder", *Acta Materialia*, Vol. 61 No. 5, pp. 1809-1819.

Tseng, P.H., Tsai, K.T., Chen, A.L. and Wang, C.C. (2019), "Performance of novel liquid-cooled porous heat sink via 3-D laser additive manufacturing", *International Journal of Heat and Mass Transfer*, Vol. 137, pp. 558-564.

Van Cauwenbergh, P., Samaee, V., Thijs, L., Nejezchlebová, J., Sedlák, P., Iveković, A., Schryvers, D., *et al.* (2021), "Unravelling the multi-scale structure–property relationship of laser powder bed fusion processed and heat-treated AlSi10Mg", *Scientific Reports*, Vol. 11 No. 1, p. 6423.

Wang, L.Z., Wang, S. and Hong, X. (2018), "Pulsed SLM-manufactured AlSi10Mg alloy: mechanical properties and microstructural effects of designed laser energy densities", *Journal of Manufacturing Processes*, Vol. 35, pp. 492-499.

Yang, P., Deibler, L.A., Bradley, D.R., Stefan, D.K. and Carroll, J.D. (2018), "Microstructure evolution and thermal properties of an additively manufactured, solution treatable AlSi10Mg part", *Journal of Materials Research*, Vol. 33 No. 23, pp. 4040-4052.

Yang, N., Luo, T., Esfarjani, K., Henry, A., Tian, Z., Shiomi, J., Chalopin, Y., *et al.* (2015), "Thermal Interface conductance between aluminum and silicon by molecular dynamics simulations", *Journal of Computational and Theoretical Nanoscience*, Vol. 12 No. 2, pp. 168-174.

Yeh, L.T. (1995), "Review of heat transfer technologies in electronic equipment", *Journal of Electronic Packaging*, Vol. 117 No. 4, pp. 333-339.

Zavala-Arredondo, M., London, T., Allen, M., Maccio, T., Ward, S., Griffiths, D., Allison, A., *et al.* (2019), "Use of power factor and specific point energy as design parameters in laser powder-bed-fusion (L-PBF) of AlSi10Mg alloy", *Materials and Design*, Vol. 182, p. 108018, doi: 10.1016/j.matdes.2019.108018.

Supplementary material

The supplementary material for this article can be found online.

Corresponding author

Scott N. Schiffres can be contacted at: sschiffr@binghamton.edu